Highly-Sensitive and High Operating Range Fully-Printed Humidity Sensors Based on BiFeO$_3$/BiOCl Heterojunctions

*Paul Fourmont, Fabrice Vaussenat, Mathieu Gratuze, Caroline A. Ross, and Sylvain G. Cloutier**

Fully-printed humidity sensors based on BiFeO$_3$/BiOCl heterojunctions fabricated using a two-step process with serigraphic printing are reported. Most importantly, this unique sensor architecture provides a broader relative humidity sensing range compared to pristine BFO sensors due to a synergistic effect between dense networks of BiOCl nanosheets synthetized atop BFO powders. With surface-to-weight ratios reaching 7.75 m^2 g^{-1}, these heterostructures increase the sensitivity and operating range of BFO-based humidity sensors. While previously reported BFO humidity sensors only detect relative humidities above 30%, The BFO/BiOCl heterojunctions can measure relative humidities as low as 15% due to their increased surface area. Optimal growth and packing of the BiOCl nanosheet/BFO powder heterostructure are achieved by tuning the loading of the BFO powder and simultaneously forming the BiOCl sheets by chemical etching and annealing of the BFO powder. Excellent performance of optimized sensors including tracking and monitoring different types of breathing are demonstrated while mounted on an oxygen mask.

1. Introduction

As a prerequisite to life, water is of paramount importance to all living organisms on the Earth. Most of the properties of the biosphere depend on the presence of water. Hence, reliable and precise determination of the amount of water vapor, or humidity in the environment is a critical parameter for many processes.[1] Some industries like cosmetics, food processing, or pharmaceuticals must carefully control humidity to avoid biological contamination and to ensure optimal properties of their

P. Fourmont, F. Vaussenat, M. Gratuze, S. G. Cloutier
Department of Electrical Engineering
École de Technologie Supérieure
1100 Notre Dame Street West, Montreal, QC H3C 1K3, Canada
E-mail: sylvaing.cloutier@etsmtl.ca

P. Fourmont, C. A. Ross
Department of Materials Science and Engineering
Massachusetts Institute of Technology
77 Massachusetts Avenue, Cambridge, MA 02139, USA

final products.[2] Materials including polymers, ceramics, or metal oxides can be used to monitor humidity.[1,3–6] Metal oxides have the advantage of being chemically and thermally stable, offering high-sensitivity, and large operating ranges,[7] and metal oxides such as ZrO$_2$, TiO$_2$, SnO$_2$, ZnO, Al$_2$O$_3$, In$_2$O$_3$, BaTiO$_3$, BiFeO$_3$ (BFO), and spinel structures have been reported as sensors.[5,8–16] They have the advantage of being nontoxic and their precursors are affordable and relatively abundant.[5] Metal oxide nanostructures can offer better-sensing properties compared to their bulk counterparts[5] due to their greater surface-to-volume ratio and specific surface area,[1,17] enabling more pronounced chemical interactions between the water molecules and the sensing material.[5,17] However, the best sensing performances are not necessarily achieved using the smallest particles as they can lead to more compact sensing layers with less available surface area.[18] In a recent study, the sensing properties of both microcubic and nanocubic BFO particles are compared and tested between 18% to 90% relative humidities (RH).[18] Faster and stronger responses are found in sensors using micron-size particles due to the increased porosity of the deposited materials and the specific surface area.[3] Another recent study reported humidity sensors based on thin films of BFO made by sol-gel, but their operating range remains limited to 30% to 90% RH, and the sensors only showed a clear capacitance change above 50% RH.[16] This implies that the dominant sensing mechanisms in BFO are likely to be based on water-phase protonic conduction since low RH values cannot be detected.[19] For this reason, synthesis of heterojunctions appears as a promising solution.[5] Heterojunctions can indeed increase the specific surface area and create depletion regions which are beneficial for humidity sensing.[5,20]

Overall, water adsorption on the sample surface is more likely to take place at low humidity conditions using porous films made of nanoparticles.[21] The morphology of the active material, including the pore sizes and volumes, can have a significant impact on the performance of a humidity sensor.[3] Still, synthesis of complex nanostructured metal oxide materials that are highly sensitive to humidity remains expensive and difficult to upscale.[1,3] To reach viable mass production, low complexity, and low production cost would be a tremendous advantage.[22,23] For volume production, such devices should possess a

minimalist architecture using only few deposition steps, (i) the conductive electrodes and (ii) the sensing material. Single-layer devices using the substrate as the active material have been reported but inferior performance is usually found.[22,24,25] In addition, whenever possible resistive sensors should be favored over capacitive-type devices as they require much simpler electronic circuit interfaces.[3,22] To fulfill and overcome the mentioned constraints, printed electronic technologies appear favorable.[23]

Printed techniques enable easier scale-up possibilities and are often more attractive as they tend to be faster and require less material compared to conventional techniques,[23] an complex printed patterns and elemental compositions are easily obtained.[26] Printed techniques such as inkjet printing or screen printing can also be readily implemented on low-cost, lightweight flexible substrates like PET or polyimide compared to conventional rigid substrates,[5] facilitating integration of devices into Internet of Things or wearable devices, including medical devices. In the context of medical care, a humidity sensor can be used to monitor the moisture of ventilated patients in intensive care.[27] During mechanical ventilation, the insufflated gas needs to be heated and humidified. A humidifier inflates the patient's lungs with a greater volume than the ventilator by raising the temperature and adding water vapor to the dry, cool gas delivered by the ventilator.[28] The relative humidity can be also used to determine respiratory parameters during the inspiration and expiration cycle.[29] Fast humidity sensors able to track such parameters have the potential to track breathing patterns in real-time and provide vital health information related to the high moisture content of human breath.[30] Other relevant pulmonary parameters such as the tidal volume, the inhale reserve volume, or the exhale respiratory volume are usually gathered to test pulmonary functions and to diagnose restrictive pulmonary diseases and obstructive lung diseases. To calculate these respiratory parameters, it is necessary to measure the evolution of respiration in real time. To obtain more precise information, a fast response of the humidity sensor without reaching the saturation state is essential.[31]

This study demonstrates all-printed and conformal BFO/BiOCl-based humidity sensors. Compared to previous BFO-based humidity sensors, this unique architecture shows a broader operating range, going from 15% to 95% relative humidity, and a resistivity change ($R_0/R_{RH} \approx 10^4$) without any poling step.[16,18,32] This performance is explained by the dense network of interconnected BFO/BiOCl heterostructures distributed all over the active surface area. The BFO powder is first made by a simple solvothermal solution and then distributed into a commercial ink vehicle for printing.[33,34] As reported in a previous study, BiOCl nanosheets can grow atop these BFO particles thanks to a thermally-activated chemical reaction between the ink vehicle and the BFO powders during annealing.[33] Moreover, we achieve a significant increase in the specific surface area (7.7×) by simply tuning the BFO loading of the printed inks. While both BiOCl and BFO have been individually used as active layers for humidity sensing devices, BiOCl/BFO heterostructures were not.[16,18,32,35] Indeed, we demonstrate that BiOCl nanosheets directly increase the operating range. As nontoxic materials, BFO/BiOCl heterostructures are compatible with medical applications,[36,37] and we successfully measured different human breathing patterns without saturating the sen-

sors. The devices are fabricated on a flexible polyimide substrate using two steps screen-printed methodology compatible with mass production allowing easy integration into wearable devices. Critical limitations faced by BFO-based humidity sensors are overcome by integrating them on a flexible substrate using a simple methodology and by improving the sensing performance through dense networks of heterojunctions.

2. Results and Discussion

Figure 1a shows the fabrication process for the humidity sensors. The first printing step is the deposition of the silver commercial ink (EDAG 725 from Henkel) to produce interdigitated silver electrodes on a flexible polyimide substrate by serigraphic printing with feature sizes of 500 µm. This technique allows the transfer of a stencil design using a squeegee and a mesh screen.[33] Only one pass of the squeegee is needed to print the interdigitated electrodes, which are then cured at 300 °C for 1 h. Figure 1b shows a single interdigitated electrode mapped by a profilometer after curing confirming that the fabrication process yields well-defined non-overlapping fingers. The histogram visible in Figure 1b shows the thickness distribution of the electrode, with average thickness ranges between 4 to 5 µm after annealing. In the supplementary Figure S1 (Supporting Information), a vertical scan over all the printed fingers is reported with an average height for the 15 fingers of ≈5 µm and widths and spacings of 500 µm. The second printing step is the deposition of the BFO ink atop the interdigitated electrodes which act as a sensing layer, followed by annealing at 300 °C to remove the ink vehicle and create BiOCl nanosheets. The synthesis of the BFO particles and the preparation of the ink formulation are fully described in a previous study, where chemical etching of the BFO powder by the ink vehicle during annealing produced dense networks of BFO/BiOCl heterostructures,[33] shown in the scanning electron microscopy (SEM) image in Figure 1c. Densely packed BiOCl nanosheets with high surface-to-volume ratio are visible atop the BFO particles. The biggest nanosheets possess a length of several microns with a thickness of only a few nanometers.[33] Compared to bare BFO powder, the dense BiOCl nanosheets increase the specific surface area, which is beneficial for the performance of the printed humidity sensors. X-ray diffraction (XRD) measurements reveal the formation of the BiOCl crystalline phase: Supplementary Figure S2 (Supporting Information) shows that BFO (ICDD 01-086-1518) and Bi_2O_3 (ICDD 01-073-6885) are present in printed layers annealed at 150 °C whereas at 300 °C, additional BiOCl (ICDD 01-083-7690) phase appears.[33,38,39]

To evaluate the benefits of the BFO/BiOCl heterostructures on the sensing performance, we started with 10 wt. % of BFO powder in the printed BFO films. We previously established that the highest annealing temperature results in the biggest and densest BFO/BiOCl heterostructures, explained by increased evaporation of the ink vehicle which contains chlorine and etches the BFO powder.[33] In Figure 2, we compare three different devices annealed at 150, 225, and 300 °C. We choose 300 °C as the maximum annealing temperature to maintain the integrity of the polyimide substrate. In Figure 2a, no BiOCl nanosheets are observed after annealing at 150 °C. Instead, BFO particles are visible but they are still partially covered by the ink vehicle. In contrast, in the printed films annealed at 225 and 300 °C, BiOCl nanosheets
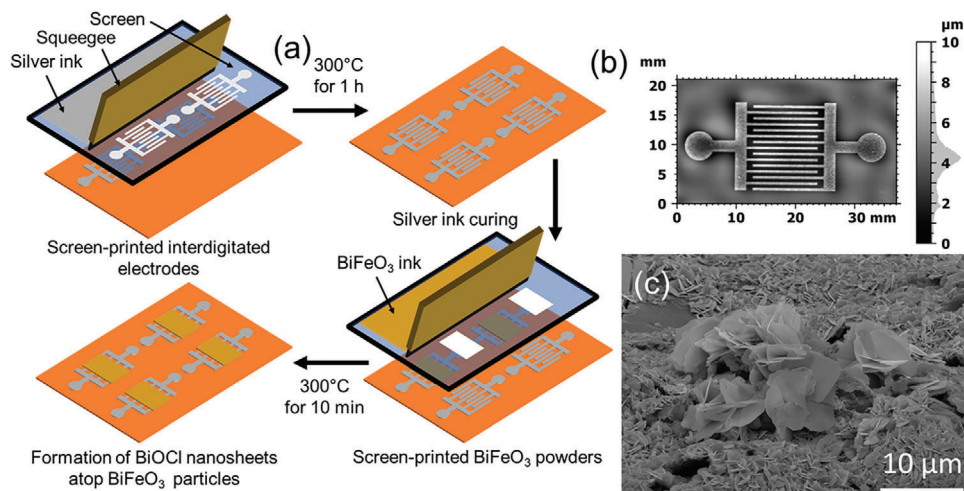
Figure 1. a) Fabrication steps of the printed BFO/BiOCl humidity sensors, b) 3D map of a screen-printed interdigitated electrodes obtained by a profilometer, and c) SEM micrograph of the BiOCl nanosheets growing atop BFO particles.

can be clearly seen, increasing with temperature. For comparison, SEM images at different magnifications for the printed ink vehicle without any BFO powder are presented in supplementary Figure S3 (Supporting Information). The printed vehicle films annealed at 300 °C are uniform with no visible features. All the printed humidity sensors were tested under the same conditions in which the humidity inside the chamber was set to 95% RH for 15 min with intervals of 15 min at 15%, 35%, 55%, and 75% RH. The test conditions from 15% to 95% RH are set to match the operating range of the chamber. Resistance values above 2×10^8 Ω are not reported as it is the limit of the data logger (Keithley 6510). As shown in Figure 2d, the printed sensors annealed at 150 °C

only detect high relative humidities ≈75% RH. Such behavior can be expected since previously reported BFO-based humidity sensors also demonstrate a clear response only above 50% RH and the BFO powder is still partially coated by a thin layer of the ink vehicle.[16,32] The electrical resistance in Figure 2d decreases while the humidity increases, as expected from a n-type material due to the electron donation from the chemically adsorbed water molecules.[19] In Figure 2e,f, both humidity sensors annealed at 225 and 300 °C show an operating range from 15% to 95% RH. The improved sensitivity at lower relative humidities is attributed to the intrinsic properties of the BiOCl nanosheets and to the higher specific surface area induced by the heterojunctions.[35]
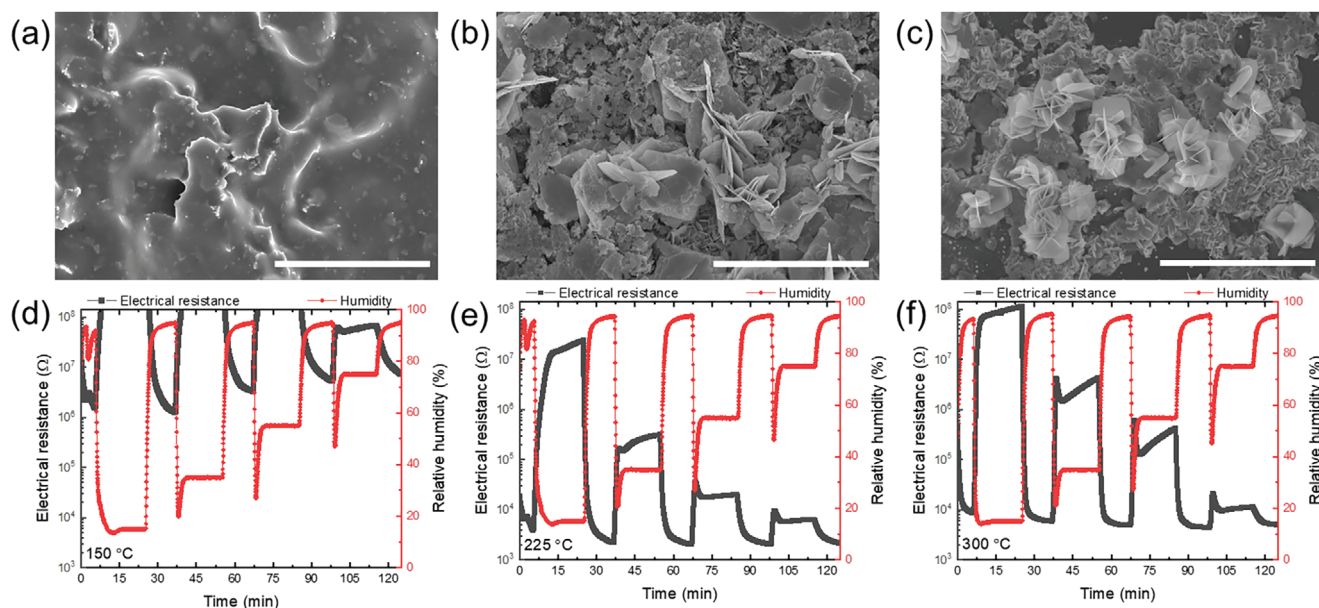

Figure 2. SEM micrographs of the printed active layers loaded with 10 wt.% BFO powder annealed at a) 150 °C, b) 225 °C, and c) 300 °C. The length of all the scalebar is 20 μm. d–f) show the variation of the electrical resistance between 15% and 95% RH over time. d,e, and f) report the performances of the active layer annealed at 150, 255, and 300 °C respectively.
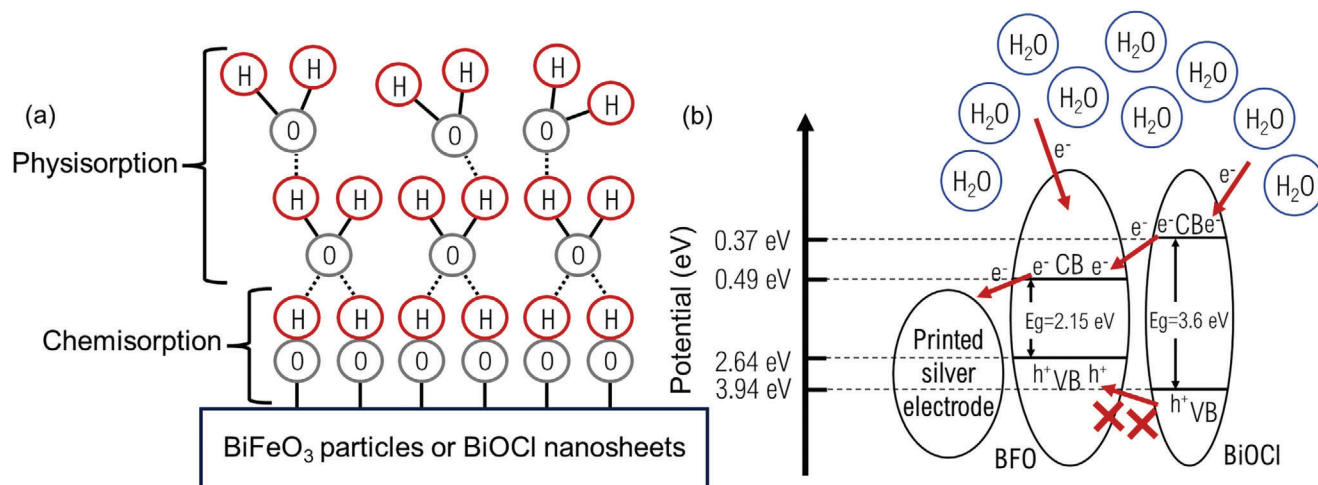
Figure 3. a) Mechanisms of water condensation on the surface of the ceramic material and b) potential band diagram of the water sensing mechanism.

The printed humidity sensors annealed at 225 and 300 °C show respectively a high response of 1.1×10^4 and 1.9×10^4 between 15% and 95% RH, where the response is the ratio of the electrical resistance of the sensors at 15% and 95% RH. As a control experiment, the ink vehicle without BFO powder was printed and annealed at 300 °C. No electrical resistance was measured and no response to humidity was detected. We previously reported that over 85 wt.% of the initial mass of the ink vehicle is evaporating after annealing above 250 °C.[33] Consequently, this result confirms that BFO/BiOCl heterojunctions alone are responsible for the humidity sensing capability.

We therefore conclude that BiOCl nanosheets are beneficial to the performance of the printed sensors. Indeed, thin films of BiOCl powder operating from 11% to 97% RH are already reported, suggesting that BiOCl is a good candidate for humidity sensing.[35] However, such sensors are produced by drop-casting method and use a quartz crystal microbalance which is not convenient for large scale deployment. In Figure 2f, a fast response of our sensor is visible when the humidity is abruptly varied ≈35%, 55%, and 75% RH. Short overshoots are detected by the sensors and are artifacts attributed to the test chamber. Nevertheless, the performances of the printed humidity sensors with 10 wt.% of BFO powder need to be optimized as the electrical resistance of the device annealed at 300 °C is not stable during each interval of 15 min at 15%, 35%, 55%, and 75% RH.

The electrical resistance from all the reported humidity sensors decreases with an increase in humidity. Such results are expected as the synthetized BFO powder is n-type.[33,40] This decrease of resistivity is attributed to the transfer of electrons from the physical adsorption and capillary condensation of water molecules on the ceramic surface.[19,41] Thus water molecules act as a reducing agent. The sensing mechanism can be described as follows: 1) the water molecules are chemically adsorbed on an active site, then 2) they form an adsorption complex which enables the creation of hydroxyl groups, and 3) subsequent water molecules are adsorbed through hydrogen bonding on two hydroxyl groups.[19] This last physisorption step is illustrated in **Figure 3**a.[19] As the RH increases more water layers condense on the surface of the sensing material. Such layers are less or-

dered and the water molecules become mobile behaving like bulk liquid water and the Grotthuss mechanism, also known as proton-hopping mechanism, becomes dominant.[19] The synergetic effect of the BFO/BiOCl heterojunctions effectively increases the surface area and the operating range for the printed humidity sensors. In Figure 3b, we propose a schematic band diagram consistent with the sensing mechanisms observed for the BFO/BiOCl humidity sensors. The BFO/BiOCl heterostructures printed atop the silver electrodes act as a sensing material. There, electrons from the BiOCl conduction band can transfer to the BFO conduction band. Then, water molecules act as reducing agents and decrease the electrical resistance of the humidity sensors. The electrons from the conduction band of the BiOCl flow to the conduction band of the BFO because the latter possesses a higher potential.[42] Finally, the printed silver electrodes act as an electron acceptor and facilitate the electron transfer from the BFO particles.[43] This flow of electrons results in a decrease of the electrical resistance when the humidity increases.

To improve the performance of the printed sensors, different loadings of BFO powder from 10 to 40 wt.% were printed, annealed at 300 °C, and tested. Figure S4 (Supporting Information) shows SEM micrographs of the printed BFO/BiOCl thin films with different BFO loadings. Low magnification Figures S4a,d,g,j (Supporting Information) show greater amounts of BFO particles as the loading is increased from 10 to 40 wt.%. At higher magnification, dense networks of BiOCl nanosheets are seen on the surfaces and edges of the BFO particles. Figures S4h,k (Supporting Information) clearly show the surface of the BFO particles with the remaining BiOCl nanosheets mostly found on the edges of the BFO particles. Finally, the highest resolution (15 000×) images are shown in Figure S4c,f,i,l (Supporting Information). In Figure S4c,f,i (Supporting Information), very dense and intricated BiOCl networks are revealed and the BFO particles are effectively etched. However, the highest loading of 40 wt.% BFO powder yields fewer BiOCl sheets compared to lower loadings (Figure S4l, Supporting Information), attributed to the lower amount of ink vehicle available to chemically react with the BFO powders to produce BiOCl nanosheets.
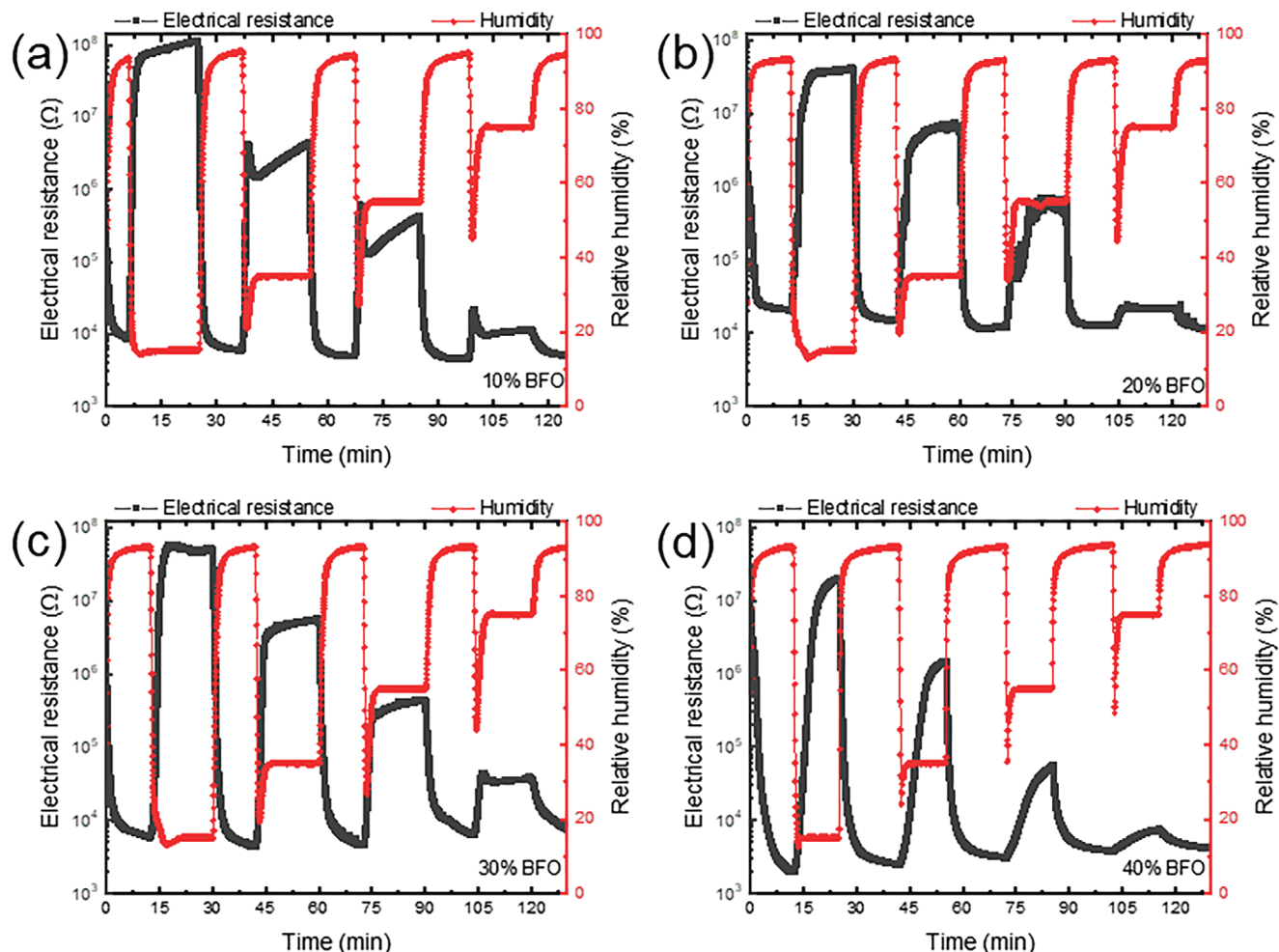
**ADVANCED
SCIENCE NEWS**

www.advancedsciencenews.com

**ADVANCED
ELECTRONIC
MATERIALS**

www.advelectronicmat.de

Figure 4. Variation of the electrical resistance over time between 15% and 95% RH of the printed humidity sensors loaded with a) 10 wt.%, b) 20 wt.%, c) 30 wt.%, and d) 40 wt.% BFO powder. All the printed active layers are annealed at 300 °C.

Brunauer-Emmett-Teller (BET) analysis provides a precise assessment of the specific surface area available for humidity sensing. The use of krypton gas allows a reliable measurement with a detection limit around one order of magnitude lower than the bare polyimide substrate.[44] Results are summarized in Table S1 (Supporting Information). Consistent with the SEM images, the 30 wt.% BFO loading shows the highest specific surface area of 7.75 m^2 g^{-1}, over 7× greater than that of 10 wt.% BFO loading. A control experiment on a bare substrate yielded a negligible specific surface area of 0.065 m^2 g^{-1}. In Figure S5 (Supporting Information), cross-section SEM micrographs of the 30 wt.% loaded sensors are presented, with thickness of 14 ± 2 μm, illustrating both BiOCl nanosheets and porosity due to the voids between the BFO particles during the printing step, which is expected to increase the performance of the humidity sensors.[18]

Figure 4 shows the effect of loading on sensor performance between 15% and 95% RH. The 10 wt.% BFO loading has poor performance: as shown in Figure 4a it does not reach a stable electrical resistance at a given relative humidity. By increasing the loadings of BFO powder to 20 and 30 wt.%, Figure 4b,c shows the electrical resistance reaching a plateau at constant humidity, with

high responses of 2.8×10^3 and 1.1×10^4 respectively for the 20 and 30 wt.% BFO-loaded films between 15% and 95% RH. In Figure 4d, the 40 wt.% BFO-loaded film displays a response of 7.6×10^3 but its electrical resistance does not stabilize at a constant humidity. The unstable responses of the 10 and 40 wt.% BFO powder below 55% RH is attributed to lower densities of BFO/BiOCl heterojunctions. In Supplementary Table S2 (Supporting Information), all the responses from the humidity sensors at different relative humidity are reported. Among all the printed sensors annealed at 300 °C, the 30 wt.% loaded has the highest response from 95% to 35% RH, 95% to 55% RH, and 95% to 75% RH.

In **Figure 5**, the electrical resistance and the sensitivity evolutions of the printed humidity sensors annealed at 300 °C are presented. In Figure 5a–c, the electrical resistances for devices with 10%, 20%, and 30% BFO loadings show an exponential response relationship in the range of 15% to 95% RH.[45] Such behavior has been shown for other ceramic-based humidity sensors and is explained by the capillary condensation of water molecules at higher relative humidity.[46,47] In Figure 5d, the sensor with 40 wt.% BFO-loading displays a different behavior. At humidities
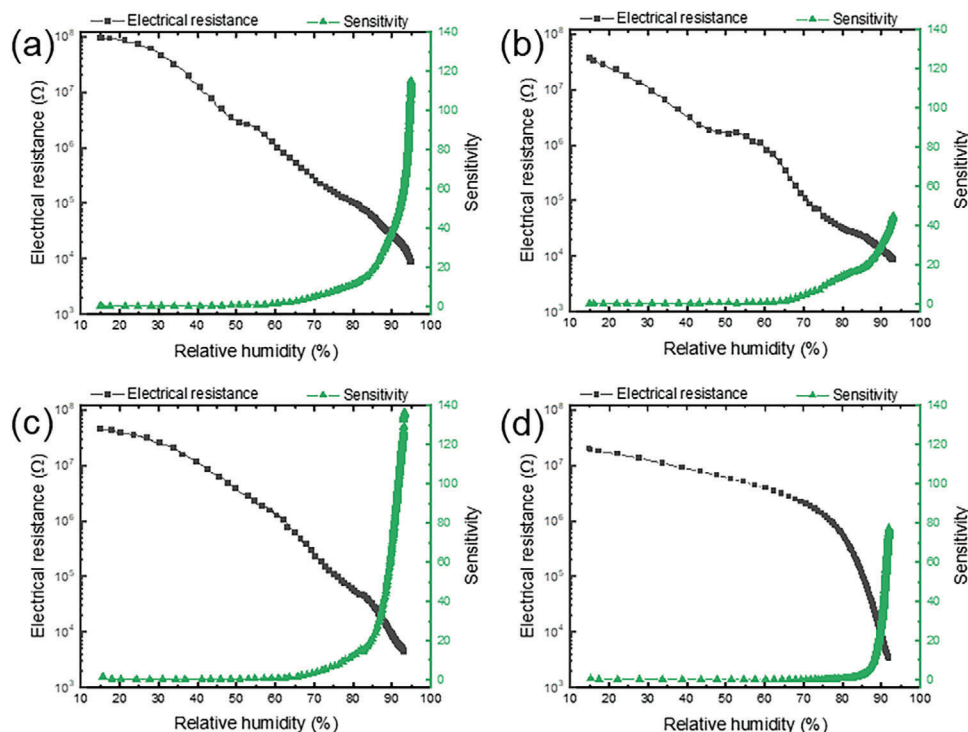
**ADVANCED
SCIENCE NEWS**

www.advancedsciencenews.com

**ADVANCED
ELECTRONIC
MATERIALS**
Open Access

www.advelectronicmat.de

Figure 5. Variation of the electrical resistance and response over the relative humidity of the printed humidity sensors loaded with a) 10 wt.%, b) 20 wt.%, c) 30 wt.%, and d) 40 wt.% BFO powder annealed at 300 °C.

below 55%, the electrical resistance slowly decreases from 20 to 5 MΩ as the RH increases. Above 55% RH, the electrical resistance rapidly decreases by more than three orders of magnitude, going from 5 MΩ to 3 kΩ. This is attributed to the lower density of BiOCl flakes leading to fewer heterojunctions to participate in the water sensing mechanism and the BFO particles dominate the response. This is consistent with previous studies reporting BFO-based humidity sensors operating above 50% RH.[16,18,32] To assess both the exponential and linear variation of the electrical resistances, a compilation of the electrical resistance all the sensors annealed at 300 °C is shown in Figure S6a (Supporting Information). The sensitivities are also presented in Figure 5, calculated as $S = R_{15\%}/(R_H \times \Delta RH)$ where $R_{15\%}$ are R_H are the electrical resistance values at 15% RH and at higher humidity while ΔRH is the variation of humidity.[18] The highest sensitivity value (137) is found for the 30% BFO-loaded devices, compared with 115, 45, and 77 for the 10%, 20%, and 40% BFO-loaded sensors respectively. In Figure S6b (Supporting Information), the sensitivities from all the sensors annealed 300 °C are reported. Above 85% RH, the 30% BFO-loaded has the highest sensitivity among all the sensors. Complex impedance measurements are presented in Supplementary Figure S7 (Supporting Information) between 100 Hz and 1 MHz measured at RH = 15–95%. All the curves have a quadrant shape and the areas under the curves tend to decrease while increasing the RH. Both the real and the imaginary parts of impedance decrease with the increase of humidity, consistent with the decrease of the electrical resistance shown in Figure 4. The printed sensor with a loading of 30 wt.% has the best performance showing the widest separation between curves at different RH.

In **Figure 6**, stability and breathing tests are shown using the optimal printed sensor using 30 wt.% BFO loading annealed at 300 °C. In Figure 6a, the transient response of the sensor is recorded over 4.5 h over consecutive cycles between 15 and 95% RH, and the hysteresis curve of one cycle is shown in Figure S8 (Supporting Information). Sudden variations of the electrical resistance are visible over time during humidification and dehumidification of the test chamber. Such important humidity changes in the chamber can take up to 20 min to increase the relative humidity from 15% to 95%. These time-consuming variations are due to the volume of the test chamber and the gas-flow rate. Such setup is not relevant to determine the real response time of the printed sensors. Fortunately, no drifting phenomenon is observed over time and the sensor shows a constant baseline. Indeed, dealing with a drifting sensor can be challenging for data postprocessing.[48] The absence of drifting allows a straightforward integration of the sensor to a facemask for real-time monitoring of different types of breathing. For validation, the optimal sensor is mounted on an oxygen mask (Hans Rudolph. 6450 series V2) as shown in the photographs in Figure 6d,e. In Figure 6b, the electrical resistance of the sensor directly mounted on the oxygen mask is reported. During the first two minutes fifteen seconds, the mask is left at ambient humidity and the electrical resistance remains constant. Following this period, the mask is fitted on the face to measure the breathing of the patient. A rapid decrease of the electrical resistance from 2 MΩ to 250 kΩ is observed during the first 45 seconds. By exhaling moisture through the mouth and nose, the sensing layer absorbs humidity from the breath and the electrical resistance decreases. After 45 s, the humidity sensor reaches a constant baseline value without
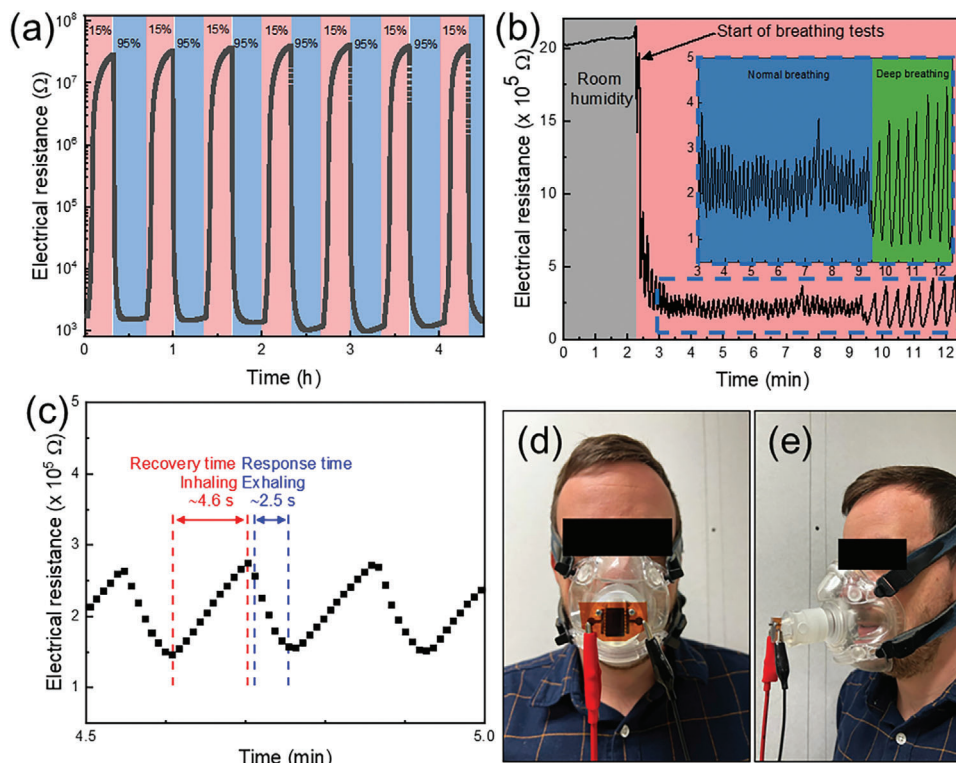
2400156 (6 of 9)

ADVANCED
SCIENCE NEWS

www.advancedsciencenews.com

ADVANCED
ELECTRONIC
MATERIALS

www.advelectronicmat.de

Figure 6. a) Stability of the optimal printed humidity sensor between 15% and 95% RH over several consecutive cycles. b) Shows the variation of the electrical resistance when the optimal sensor is mounted on an oxygen mask. The inset demonstrates that the sensor can monitor different types of breath. c) Exhibits the inhaling and exhaling part of the breath. Such a figure allows to determine the recovery and the response time of the sensor. d,e) Photographs of the breathing monitoring setup used to assess different types of breathing.

reaching a saturated state. The inset of Figure 6b confirms that different types of breathing (normal and deep breathing) can be accurately measured by the humidity sensor. Variations of electrical resistances induced by normal and deep breathings are respectively ≈125 and 300 kΩ. Such results can be expected as deeper breathing induces larger humidity variations compared to normal breathing.[49] Hence, an adequate response time from the sensor allows the breathing phases to be distinguished, an essential characteristic in medical devices to constantly monitor the vital parameters of the wearer.[27] Further analysis of the normal breathing in Figure 6c allows the determination of the recovery and response time constants. A recovery time of 4.6 s and a response time of 2.5 s can be measured for the optimal printed sensor configuration. These two durations are obtained while inhaling and exhaling normally.

In Table S3 (Supporting Information), we compare the performance of our sensor with previously reported humidity sensors based on perovskite structures. Various structures such as $LaCoO_3$,[50] $SrTiO_3$,[51–53] $NaTaO_3$,[54] $Ba_{0.8}Sr_{0.2}TiO_3$,[55] $LaFeO_3$,[56] $LaVO_3$,[57] $NiVO_3$[57] have been tested. Such results demonstrate that perovskites are suitable for humidity sensing. However, most of the reported studies do not involve up scalable and industry-compatible techniques which hinders the integration of such structures to commercial devices. As summarized in **Table 1**, our BFO-based humidity sensors possess a higher operating range compared to the reported humidity sensors using BFO as an active sensing material. Our sensors also have the advantage of being flexible and lightweight, which is beneficial for wearable applications.[58] In addition, the fabricated sensors are the only all printed devices reported in Table 1. By using two steps

Table 1. Comparison of the performances of the humidity sensors using BFO as an active layer material.

Deposition method	Substrate	Type	Operating range [% RH]	Response [R_o/R_{RH}]	Sensitivity [Resp/ΔRH]	Response time/ recovery time [s]	Reference
Drop casting (BFO)	Copper spiral electrodes	Impedance (at 1 kHz)	16–92	46.8	0.61	50/150	Douani 2020
Drop casting (BFO/CFs)				126.5	1.66	130/75	
Spin-coating	Pt/Si(111)	Capacitive	30–90	56.4	0.94	60/70	Zhang 2022
Screen printing	Al_2O_3	Resistive	30–95	3×10^4	450	0.084/0.376	Chen 2022
Screen printing	Kapton	Resistive	15–95	1.1×10^4	137	2.5/4.6	This work

screen-printing methodology, we ensure that the proposed devices can be manufactured using pilot- and manufacturing-grade equipment. Such characteristics are essential to scale up the manufacturing process and capability.

3. Conclusion

This study reports for the first time highly-sensitive and high operating range all printed humidity sensors based on dense networks of BFO/BiOCl heterojunctions. The sensors are fabricated on flexible polyimide substrate using a two-step serigraphic (screen-printing) process. We demonstrate that BiOCl nanosheets growing atop BFO particles prove beneficial to extend the operating range. Compared to a state-of-the-art BFO sensor which can effectively sense humidity only above 50% RH, we report BFO/BiOCl-based humidity sensors operating from 15% to 95% RH. We show that loading of 30 wt.% of BFO powder yields the densest networks of BFO/BiOCl heterojunctions and the highest specific surface area of 7.75 m^2 g^{-1}, and these optimized sensors display a high response >10^4 and a sensitivity of 137. Compared to BFO-based humidity sensors reported in the literature, these sensors exhibit the highest operating range reported yet. We demonstrate their use as a suitable device to detect and monitor human breathing when mounted on a facemask. Thanks to its suitable response time, different types of breathing can be detected by the sensor. Such characteristics are essential for medical applications to extract vital breathing parameters.

4. Experimental Section

Materials: BFO powder is synthetized using a straightforward solvothermal methodology already reported.[33,34] The printed ink was obtained by mixing the BFO powder with a commercial ink vehicle from Henkel (SOL725).[33] The BFO was dispersed in the ink vehicle using a planetary centrifugal mixer to ensure a good homogeneity of the inks. A maximum of 40 wt.% BFO powder could be introduced before reaching saturation of the ink vehicle. Above this amount, the BFO powder started to form clusters and the ink was no longer homogeneous. A 325-mesh size was used to print both the interdigitated electrodes and the BFO-based active layer. Both layers were printed on 200 µm thick polyimide substrate using screen printing technique (P200S from KEKO). Each layer was cured in a reflow oven (MC301N, Manncorp) at 300 °C in an ambient atmosphere. The silver layer was annealed for 1 h and the BFO sensing layer was annealed for 10 min. The silver interdigitated electrodes are printed using a commercially available ink from Henkel (EDAG725).

Characterizations: The 3D map of the screen-printed interdigitated silver electrodes was measured using a surface profilometer (P17, KLA Tencor). Micrographs of the humidity sensors were obtained by scanning electron microscopy (SU8230, Hitachi) to assess the growth of the BiOCl nanosheets on the BFO particles. All the printed humidity sensors were tested using an environmental chamber (Peltier type sample stage, Nextron) coupled with humidity and temperature control systems. The temperature for all the experiments was set to 25 °C. The variations of electrical resistance of the printed humidity sensors are recorded using a data acquisition unit (DAQ6510, Keithley). Specific surface area measurements were performed using the Brunauer-Emmett-Teller (BET) technique (Tristar II Plus, Micromeritics). The samples were pre-dried and degassed at 140 °C for 12 h before each measurement. Adsorption–desorption isotherms of the thin films were measured at 77K with krypton gas. X-ray diffraction patterns of the BFO and BFO/BiOCl heterojunctions were collected on a Bruker D8 Advance equipped with Cu Kα monochromatic source.

Supporting Information

Supporting Information is available from the Wiley Online Library or from the author.

Conflict of Interest

The authors declare no conflict of interest.

Author Contributions

P.F. directed the research, conceived the idea, and designed the research; P.F. printed all the sensors used in this study and performed the measurements; M.G. participated in the data acquisition using the profilometer and the environmental chamber; F.V. helped with the measurements regarding the oxygen mask. The first version of the manuscript was written by P.F. Valuable corrections and comments on the manuscript were done by S.G.C., C.A.R., F.V., and M.G.

Data Availability Statement

The data that support the findings of this study are available on request from the corresponding author. The data are not publicly available due to privacy or ethical restrictions.

Ethics Declarations

The institutional ethics board of École de Technologie Supérieure (ÉTS) approved this study (certificate number H20231007). The data and photographs were recorded with the informed consent of the participants.

[1] J. Wang, W. Zeng, A. J. Palma, *J. Sens.* **2022**, *2022*, 1.

[2] G. M. Patel, V. R. Shah, G. J. Bhatt, P. T. Deota, *Nanosens. Smart Manuf.* **2021**, 555.

[3] T. A. Blank, L. P. Eksperiandova, K. N. Belikov, *Sens. Actuators, B* **2016**, *228*, 416.

[4] W. Gu, H. Zhang, C. Chen, J. Zhang, *Curr. Appl. Phys.* **2022**, *34*, 112.

[5] D. Nunes, A. Pimentel, A. Gonçalves, S. Pereira, R. Branquinho, P. Barquinha, E. Fortunato, R. Martins, *Semicond. Sci. Technol.* **2019**, *34*, 43001.

**ADVANCED
SCIENCE NEWS**

www.advancedsciencenews.com

**ADVANCED
ELECTRONIC
MATERIALS**

www.advelectronicmat.de

[6] X. Wang, O. Larsson, D. Platt, S. Nordlinder, I. Engquist, M. Berggren, X. Crispin, *Sens. Actuators B* **2012**, *166*, 556.

[7] M. V. Nikolic, Z. Z. Vasiljevic, M. D. Lukovic, V. P. Pavlovic, J. B. Krstic, J. Vujancevic, N. Tadic, B. Vlahovic, V. B. Pavlovic, *Int. J. Appl. Ceram. Technol.* **2019**, *16*, 981.

[8] J. Wang, M.-Y. Su, J.-Q. Qi, L.-Q. Chang, *Sens. Actuators, B* **2009**, *139*, 418.

[9] J. Wang, X.-H. Wang, X.-d. Wang, *Sens. Actuators, B* **2005**, *108*, 445.

[10] C.-N. Xu, K. Miyazaki, T. Watanabe, *Sens. Actuators, B* **1998**, *46*, 87.

[11] D.-U. Kim, M.-S. Gong, *Sens. Actuators, B* **2005**, *110*, 321.

[12] X. Liu, R. Wang, T. Zhang, Y. He, J. Tu, X. Li, *Sens. Actuators, B* **2010**, *150*, 442.

[13] Q. Qi, T. Zhang, Q. Yu, R. Wang, Y. Zeng, L. Liu, H. Yang, *Sens. Actuators, B* **2008**, *133*, 638.

[14] M. Vilaseca, J. Coronas, A. Cirera, A. Cornet, J. R. Morante, J. Santamaria, *Sens. Actuators, B* **2007**, *124*, 99.

[15] S. Basu, S. Chatterjee, M. Saha, S. Bandyopadhay, K. K.r Mistry, K. Sengupta, *Sens. Actuators, B* **2001**, *79*, 182.

[16] Y. Zhang, B. Li, Y. Jia, *Materials* **2022**, *15*, 2932.

[17] R. Si, X. Xie, T. Li, J. Zheng, C. Cheng, S. Huang, C. Wang, *ACS Sens.* **2020**, *5*, 1345.

[18] X. Chen, C. Liu, Z. Hua, N. Ma, *ACS Appl. Mater. Interfaces* **2022**, *14*, 49965.

[19] Z. Chen, C. Lu, *Sens. Lett.* **2005**, *3*, 274.

[20] Y. Lu, K. Xu, L. Zhang, M. Deguchi, H. Shishido, T. Arie, R. Pan, A. Hayashi, L. Shen, S. Akita, K. Takei, *ACS Nano* **2020**, *14*, 10966.

[21] S. Kano, J. Kawakita, S. Yamashita, H. Mekaru, *Chemosensors* **2023**, *11*, 564.

[22] D. Barmpakos, G. Kaltsas, *Sensors* **2021**, *21*, 739.

[23] Q. Li, J. Zhang, Q. Li, G. Li, X. Tian, Z. Luo, F. Qiao, X. Wu, J. Zhang, *Front. Mater.* **2019**, *5*, 77.

[24] P. M. Harrey, B. J. Ramsey, P. S. A. Evans, D. J. Harrison, *Sens. Actuators, B* **2002**, *87*, 226.

[25] Y. Kim, B. Jung, H. Lee, H. Kim, K. Lee, H. Park, *Sens. Actuators, B* **2009**, *141*, 441.

[26] F. Villani, P. Vacca, G. Nenna, O. Valentino, G. Burrasca, T. Fasolino, C. Minarini, D. della Sala, *J. Phys. Chem. C* **2009**, *113*, 13398.

[27] F. Vaussenat, A. Bhattacharya, J. Payette, J. A. Benavides-Guerrero, A. Perrotton, L. F. Gerlein, S. G. Cloutier, *JMIR Biomed. Eng.* **2023**, *8*, e47146.

[28] G. A. Plotnikow, M. Accoce, E. Navarro, N. Tiribelli, *Rev. Bras. Ter. Intensiva* **2018**, *30*, 86.

[29] L. Ma, R. Wu, A. Patil, S. Zhu, Z. Meng, H. Meng, C. Hou, Y. Zhang, Q. Liu, R. Yu, J. Wang, N. Lin, X. Y. Liu, *Adv. Funct. Mater.* **2019**, *29*, 1904549.

[30] S. Kano, N. Jarulertwathana, S. Mohd-Noor, J. K. Hyun, R. Asahara, H. Mekaru, *Sensors* **2022**, *22*, 3.

[31] H. Yan, L. Zhang, P. Yu, L. Mao, *Anal. Chem.* **2017**, *89*, 996.

[32] R. Douani, N. Lamrani, M. '. H. Oughanem, M. Saidi, Y. Guhel, A. Chaouchi, B. Boudart, *Sens. Actuators, A* **2020**, *307*, 111981.

[33] P. Fourmont, S. G. Cloutier, *RSC Adv.* **2022**, *12*, 24868.

[34] P. Fourmont, Y. Bai, F.-X. Fortier, S. G. Cloutier, *ACS Appl. Electron. Mater.* **2022**, *4*, 5905.

[35] Q. Chen, N.-B.o Feng, X.-H.e Huang, Y. Yao, Y.-R. Jin, W. Pan, D. Liu, *ACS Omega* **2020**, *5*, 18818.

[36] A. Rajaee, S. Wang, L. Zhao, Y. Liu, *J. Phys.: Conf. Ser.* **2019**, *1305*, 012046.

[37] H. Ijaz, R. Zia, A. Taj, F. Jameel, F. K. Butt, T. Asim, N. Jameel, W. Abbas, M. Iqbal, S. Z. Bajwa, W. S. Khan, *Appl. Nanosci.* **2020**, *10*, 3569.

[38] C. Ponraj, G. Vinitha, J. Daniel, *Int. J. Green Energy* **2019**, *17*, 71.

[39] C. Ponzoni, R. Rosa, M. Cannio, V. Buscaglia, E. Finocchio, P. Nanni, C. Leonelli, *J. Alloys Compd.* **2013**, *558*, 150.

[40] P. Fourmont, R. Nechache, S. G. Cloutier, *ACS Appl. Nano Mater.* **2021**, *4*, 12261.

[41] J. F. Boyle, K. A. Jones, *J. Electron. Mater.* **1977**, *6*, 717.

[42] H. Yang, *Mater. Res. Bull.* **2021**, *142*, 111406.

[43] P. V. Kamat, *J. Phys. Chem. C* **2007**, *111*, 2834.

[44] J. Rouquerol, F. Rouquerol, P. Llewellyn, G. Maurin, K. Sing, *Adsorption by Powders and Porous Solids: Principles, Methodology and Applications*, Academic press, Cambridge, USA **2013**.

[45] G. Chaloeipote, J. Samarnwong, P. Traiwatcharanon, T. Kerdcharoen, C. Wongchoosuk, *R. Soc. Open Sci.* **2021**, *8*, 210407.

[46] J. Herrán, I. Fernández, E. Ochoteco, G. Cabañero, H. Grande, *Sens. Actuators, B* **2014**, *198*, 239.

[47] P. M. Faia, C. S. Furtado, A. J. Ferreira, *Sens. Actuators, B* **2004**, *101*, 183.

[48] S. Feng, F. Farha, Q. Li, Y. Wan, Y. Xu, T. Zhang, H. Ning, *Sensors* **2019**, *19*, 3760.

[49] Y. Wang, L. Zhang, Z. Zhang, P. Sun, H. Chen, *Langmuir* **2020**, *36*, 9443.

[50] E. E. Ateia, A. T. Mohamed, M. Morsy, *J. Mater. Sci.: Mater. Electron.* **2019**, *30*, 19254.

[51] D. Li, J. Zhang, L. Shen, W. Dong, C. Feng, C. Liu, S. Ruan, *RSC Adv.* **2015**, *5*, 22879.

[52] L. T. Duy, J.-Y. Baek, Y.-J. Mun, H. Seo, *J. Mater. Sci. Technol.* **2021**, *71*, 186.

[53] A. Ahmed, A. M. Soomro, D. Kumar, M. Waqas, K. H. Memon, F. Ahmed, S. Kumar, H. Ashraf, K. H. Choi, *Sensors* **2022**, *23*, 401.

[54] Y. Zhang, Y.u Chen, Y. Zhang, X. Cheng, C. Feng, L. Chen, J. Zhou, S. Ruan, *Sens. Actuators, B* **2012**, *174*, 485.

[55] Y. Xia, T. Fei, Y. He, R. Wang, F. Jiang, T. Zhang, *Mater. Lett.* **2012**, *66*, 19.

[56] J. Zhao, Y. Liu, X. Li, G. Lu, L.u You, X. Liang, F. Liu, T. Zhang, Y.u Du, *Sens. Actuators, B* **2013**, *181*, 802.

[57] S. Rajmohan, A. Manikandan, V. Jeseentharani, S. Arul Antony, J. Pragasam, *J. Nanosci. Nanotechnol.* **2016**, *16*, 1650.

[58] Z. Duan, Z. Jiang, H. Tai, *J. Mater. Chem. C* **2021**, *9*, 14963.